

Deformable and rigid registration of MRI and microPET images for photodynamic therapy of cancer in mice

Baowei Fei^{a)}

Department of Radiology, Case Western Reserve University and University Hospitals of Cleveland, Cleveland, Ohio 44106 and Department of Biomedical Engineering, Case Western Reserve University, Cleveland, Ohio 44106

Hesheng Wang

Department of Biomedical Engineering, Case Western Reserve University, Cleveland, Ohio 44106

Raymond F. Muzic, Jr.

Department of Radiology, Case Western Reserve University and University Hospitals of Cleveland, Cleveland, Ohio 44106 and Department of Biomedical Engineering, Case Western Reserve University, Cleveland, Ohio 44106

Chris Flask

Department of Radiology, Case Western Reserve University and University Hospitals of Cleveland, Cleveland, Ohio 44106

David L. Wilson

Departments of Biomedical Engineering and Radiology, Case Western Reserve University, University Hospitals of Cleveland, Cleveland, Ohio 44106

Jeffrey L. Duerk

Department of Radiology, Case Western Reserve University and University Hospitals of Cleveland, Cleveland, Ohio 44106 and Department of Biomedical Engineering, Case Western Reserve University, Cleveland, Ohio 44106

Denise K. Feyes and Nancy L. Oleinick

Department of Radiation Oncology, Case Western Reserve University and University Hospitals of Cleveland, Cleveland, Ohio 44106

(Received 11 July 2005; revised 8 December 2005; accepted for publication 9 December 2005; published 23 February 2006)

We are investigating imaging techniques to study the tumor response to photodynamic therapy (PDT). Positron emission tomography (PET) can provide physiological and functional information. High-resolution magnetic resonance imaging (MRI) can provide anatomical and morphological changes. Image registration can combine MRI and PET images for improved tumor monitoring. In this study, we acquired high-resolution MRI and microPET ¹⁸F-fluorodeoxyglucose (FDG) images from C3H mice with RIF-1 tumors that were treated with Pc 4-based PDT. We developed two registration methods for this application. For registration of the whole mouse body, we used an automatic three-dimensional, normalized mutual information algorithm. For tumor registration, we developed a finite element model (FEM)-based deformable registration scheme. To assess the quality of whole body registration, we performed slice-by-slice review of both image volumes; manually segmented feature organs, such as the left and right kidneys and the bladder, in each slice; and computed the distance between corresponding centroids. Over 40 volume registration experiments were performed with MRI and microPET images. The distance between corresponding centroids of organs was 1.5 ± 0.4 mm which is about 2 pixels of microPET images. The mean volume overlap ratios for tumors were 94.7% and 86.3% for the deformable and rigid registration methods, respectively. Registration of high-resolution MRI and microPET images combines anatomical and functional information of the tumors and provides a useful tool for evaluating photodynamic therapy. © 2006 American Association of Physicists in Medicine.
[DOI: 10.1118/1.2163831]

Key words: deformable image registration, photodynamic therapy, finite element model, small animal imaging, cellular and molecular imaging and cancer

I. INTRODUCTION

Photodynamic therapy (PDT) is a promising and relatively new therapeutic modality for cancer treatment.¹ With PDT, a tumor-localized photosensitizer is irradiated with visible light to generate reactive oxygen that efficiently kills cells

and ablates tumors.¹ PDT can be administered deep into tumors using minimally invasive techniques as only the small laser fiber that delivers the light to the tumor needs to be inserted into the lesion. PDT with Photofrin is US-FDA approved for treating early and advanced lung cancer, advanced

esophageal cancer, and Barrett's esophagus.¹ PDT requires (a) a photosensitizer, often a porphyrin-related macrocycle, that tends to accumulate in tumors; (b) nonthermal visible light of a wavelength absorbed by the photosensitizer and generally in the red region of the spectrum; and (c) molecular oxygen. With an adequate oxygen supply and light intensity, the site of photodamage depends on the location of the photosensitizer. An important advantage of PDT is that both the photosensitizer and the light are inert by themselves, and the light can be precisely focused onto a selected region, allowing extreme specificity in the localization of the photodynamic effect. Consequently, systematic toxicities are minimized.

Imaging techniques provide a powerful tool for assessing PDT efficacy. First, use of positron emission tomography (PET) with ¹⁸F-fluorodeoxyglucose (FDG) to image mice after PDT has shown that the tumor FDG uptake 15 min after PDT was a direct measurement of tumor metabolism as reported by our group² and others.³ Second, magnetic resonance imaging (MRI) has been used to evaluate PDT-induced vascular damage followed by hemorrhagic necrosis in murine M1 tumors in mice.⁴ Blood oxygenation level-dependent (BOLD) contrast MRI shows attenuation (25%–40%) of MR signal at the treated tumor site.⁵ Decreases in contrast agent uptake rates following PDT were observed by gadolinium contrast MRI.⁶ Third, *in vivo* ³¹P nuclear magnetic resonance (NMR) has been used to monitor tumor metabolic status before and after the treatment of RIF-1 tumors^{7,8} and mammary carcinoma.^{9,10} During PDT treatment, significant decreases were observed for the nucleoside triphosphate concentrations, and tumor pH, while inorganic phosphate concentrations increased.⁷ The NMR data revealed significant differences in the time course of high-energy phosphate levels in combined hyperthermia and photodynamic therapies.⁹ It was also demonstrated that there is a relationship between NMR measurements immediately following PDT and the ultimate effect on the tumor.⁸ Significant increases in T1s of water protons were observed after PDT treatment.⁸ Fourth, diffusion-weighted MRI showed a biphasic change in the apparent diffusion coefficient (ADC) within the first 24 h post-PDT, indicating the early response of PC-14 tumors to PDT.¹¹ Finally, diffuse optical measurement has been used to monitor PDT dosimetry in the human prostate.^{12,13}

In this study, we are combining multiple imaging modalities for monitoring PDT efficacy. For example, PET can image the rapid biochemical and physiological responses of tumors to PDT whereas MRI provides superior assessment of anatomical information, location, and morphological changes within tumors. Combining PET and MRI has several advantages. (1) MRI scans provide anatomical reference for the PET images. (2) Fusion of MRI and PET images can enhance our ability to visualize the distribution of a radiolabeled pharmaceutical. (3) MRI provides tumor shape and size information that can be used to improve the accuracy of the PET data analysis, such as drawing regions of interests (ROIs) and performing quantitative analyses. (4) MRI can be used to correct PET data for partial volume effects to clarify

that the PET-measured changes induced by PDT are due to metabolic and hemodynamic changes and not to artifacts of changes in tumor size.

In this paper, we focus on multimodality image registration methods for high-resolution MRI and microPET. Rigid-body registration algorithms for MRI and PET images have been used for human brain,^{14–20} for the rat brain,^{21,22} and for the cat brain.²³ Deformable registration is required whenever the subject is in different positions or the organ is deformed.²⁴ Finite element models (FEMs) have been used for registration of the brain,^{25,26} the lung,²⁷ the prostate,²⁸ and coronary arteries.²⁹ These methods were applied to register images from the same modality. Thin-plate spline based registration techniques were reported by us³⁰ as well as others.^{31–33} These methods were mainly used for human image registration.

When applying the current methods to multimodality mouse registration, several challenges arise because (1) there are significant physiological and anatomic differences between human and mice; (2) a mouse is 500 times smaller than a human; (3) the mouse body is very flexible and thus often deforms between imaging procedures; and (4) functional images, such as PET, are very different from anatomic MR images in regard to their lower resolution and fewer anatomic features. To the best of our knowledge, there is no report on deformable registration of mouse MRI and microPET images.

In this study, we performed microPET and MR imaging experiments on mice undergoing PDT. We developed two registration methods for this particular application. We conducted over 40 registration experiments and reported the evaluation results from visual inspection and quantitative measurements.

II. MATERIALS AND METHODS

A. Animal preparation

RIF (radiation-induced fibrosarcoma)-1 cells were grown as monolayers in E-MEM supplemented with 15% fetal bovine serum.³⁴ Prior to inoculation, C3H/HeN mice were shaved and depilated. Two tumors were initiated in each mouse by injection of 10⁵–10⁶ RIF-1 cells intradermally on the shoulder flanks, as far from the bladder and kidneys as possible to minimize confounding artifacts in PET images.

Tumors were treated and imaged when they reached 3–5 mm in diameter, which required 7–10 days after implantation. Animals were given the photosensitizer Pc 4 (1 mg/kg) by tail vein injection. We know from experience that neither the light nor the photosensitizer alone produces any response. After 48 h, one of the two tumors was exposed to red light (670 nm) from a diode laser (150 J/cm²; 150 mW/cm²). The other tumor in each animal served as a control (receiving photosensitizer but no light). The animals were also studied by microPET and MR imaging.

Figure 1 shows the procedure for the PDT and imaging experiment. In summary, 48 h after the Pc 4 injection, the mouse was scanned by MRI and then immediately transported to a PET system for a transmission scan. The animal

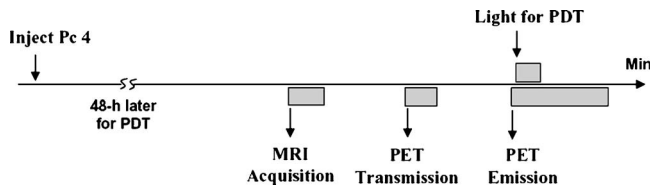


FIG. 1. Protocol for the photodynamic therapy and imaging experiment. Forty-eight hours after the injection of the photosensitizing drug Pc 4, the animal was scanned by MRI and then was immediately transported to the PET facility for a transmission scan. The animal was injected with FDG and PET emission images were acquired for a period of 90 min. Six minutes after the FDG injection, the tumor was illuminated by laser light for therapy for 15 min.

was then injected with ^{18}F -fludeoxyglucose (FDG). PET emission images were immediately acquired for a period of 90 min. About 6 min after the FDG injection, one tumor was exposed to laser light for 15 min. During the PDT and imaging session, the animals were mounted on a plastic holder and were provided with a continuous supply of 2% isoflurane (EZAnesthesia, Palmer, PA) in oxygen to minimize motion artifacts in MR images.

B. Image acquisitions

Two days after photosensitizer injection, the animals were taken to the imaging facility. The mouse MR images were acquired using a Siemens Sonata 1.5 T scanner (Siemens Medical Systems, Erlangen, Germany). A dedicated custom-designed whole-body mouse coil (two-element phased-array, i.d.=32 mm) was used to minimize noise levels. A T1-weighted spin echo pulse sequence (TR/TE=600/13 ms) with a slice thickness of 1 mm was used to generate high-resolution coronal images (matrix: 256×120 , FOV: 80×36 mm, pixel size: 0.3×0.3 mm). The acquisition time for an image slice was 72 s. In these T1-weighted images, the tumors are clearly delineated by the bright subcutaneous fat signal. We acquired three to five MR image volumes from each mouse.

After MR image acquisition, the animals and the laser system were taken to the PET imaging facility. We used a microPET R4 scanner (Concorde Microsystems, Inc., Knoxville, TN 37932) designed specifically for imaging small rodents.³⁵ We followed a single animal over a 90 min period of time and monitored the response to PDT and the outcome. We used ^{18}F -FDG that is the standard radiopharmaceutical used in PET scanning for tumor diagnosis and assessment. It was produced for this experiment in standard fashion. We acquired both transmission and emission images from the same mouse. Since the animal was anesthetized and remained in the same position during the imaging session, we assume that there was no movement between the PET transmission and emission scans. One PET image volume includes 63 transverse slices covering the whole mouse and each slice has 128×128 pixel with an in-plane pixel size of 0.85×0.85 mm and a thickness of 1.2 mm. From each mouse, we acquired 10 to 22 dynamic PET image volumes.

The total FDG activity for the period of 90 min was also computed to create another PET image volume. We used these volumes for registration experiments.

C. Image preprocessing

We used interpolation to create isotropic MR volumes before registration. The input MR volume is a 2D MR acquisition with a pixel size of 0.3×0.3 mm and a slice thickness of 1.0 mm. Twenty-nine coronal slices cover the whole mouse. Using a sinc interpolation, we created isotropic voxels of 0.3 mm on a side for both PET and MR image volumes. We use IDL (Interactive Data Language, Research System Inc., Boulder, CO) as the programming language.

We normally discretized the PET data to 256 gray levels for image display and processing. We use the scaled data for NMI registration. We also examined registration performance using different intensity scaling such as 512, 256, 128, 64, or 32 bins for both volume data sets. Scaling was linear between zero and the maximum value. Registration quality was analyzed by NMI values and by visual inspection.

For the purposes of deformable registration, we optionally cropped image slices that were not of interest. In the present case, because the tumors were on the mouse back near the shoulder, we cropped out images at the head and abdomen. For example, a typical image volume was $350 \times 250 \times 250$ voxel covering the whole mouse before cropping. After cropping, we created a volume with $148 \times 80 \times 90$ voxel near the region of interest. Cropping can bring two advantages for the tumor registration. First, cropping out regions that are not of interest can increase image consistency for the mutual information registration. Since the mouse body is very flexible, the deformation at the abdomen can cause inconsistency for the registration. Second, the small number of voxels after cropping can increase the speed of image registration.

D. Automatic whole body registration

For alignment of the whole mouse body, we used an automatic three-dimensional (3D) rigid-body registration algorithm. Based on our previous experience,^{30,36–40} we chose normalized mutual information (NMI) as the similarity measure for the rigid-body registration. This is because it does not require a linear relationship between the intensity values of the two images and it is suitable for multimodality image registration.⁴¹ One image R is the *reference* and the other F is *floating*. Their normalized mutual information (NMI) is given by the following equation.⁴²

$$\text{NMI}(R, F) = \frac{2MI(R, F)}{H(R) + H(F)},$$

where

$$H(R) = - \sum_r p_R(r) \log p_R(r),$$

$$H(F) = - \sum_f p_F(f) \log p_F(f),$$

$$MI(R, F) = - \sum_{r, f} p_{RF}(r, f) \log \frac{p_{RF}(r, f)}{p_R(r) \cdot p_F(f)}.$$

The joint probability $p_{RF}(r, f)$ and the marginal probabilities $p_R(r)$ of the reference image and $p_F(f)$ of the floating image can be estimated from the normalized joint intensity histograms. When two images are geometrically aligned, NMI is maximal.⁴²

We combined the PET transmission and emission images and formed one data set by taking a weighted sum. We then used the combined PET data and the high-resolution MR image for the registration of whole mouse body. The transmission images provide anatomic information to aid in the NMI registration. We use the MRI data as the floating images because they have higher resolution as compared to the PET images. We used rigid-body transformation (three translations and three rotations) and trilinear interpolation as described previously.⁴³ For optimization, we used the downhill simplex method of Nelder and Mead.⁴⁴ Optimization of similarity ends either when the maximum number (800) of calculations is reached or the fractional change in similarity function is smaller than a tolerance (0.001). Typically the latter is achieved within about 200 iterations. Our first initial guess is all zeros for the three displacements and three angles.

E. Deformable tumor registration

For tumor registration, we developed a finite element model (FEM)-based deformable registration method. We first cropped both MRI and microPET images. The cropped images covered only the tumor region. As MRI and microPET image volumes have different image resolutions, they were interpolated using a sinc interpolation method.⁴⁵ The isotropic voxel size of both images was 300 μm after interpolation.

At the first step, we applied the rigid NMI-based registration algorithm to align the cropped MRI and microPET images using three translations and three rotations. After registration, we manually segmented the tumor slice-by-slice on both high-resolution MRI and microPET image volumes.

We then applied the deformable registration algorithm. For a linear elastic continuum with no initial stresses and strains, the deformation energy E of an elastic body submitted to externally applied forces can be expressed as²⁵

$$E = \frac{1}{2} \int_{\Omega} \sigma^T \varepsilon \, d\Omega + \int_{\Omega} F u \, d\Omega$$

where u is the displacement vector, Ω is the elastic body, σ is the stress vector, ε is the strain vector, and F is the force applied to the elastic body. For a material with the maximum symmetry, i.e., an isotropic material, the material properties are the same in every direction. There are only two independent parameters for the stress and strain vectors (σ and ε): the Young's modulus that relates tension and stretch, and the Poisson ratio that is the ratio of the lateral contraction due to the longitudinal stretch.

The displacement field u within each element is approximated as an assembly of discrete elements interconnected at the nodal points on the element boundaries. The elements we used are tetrahedra for the volumes and triangles for the surfaces. We built the meshes for the tumor surfaces using commercial software AMIRA (Mercury Computer Systems, Inc., Chelmsford, MA). The tumor surfaces were then imported to the finite element analysis software FEMLAB (COMSOL, Inc., Burlington, MA). The tumor defined by the surface is partitioned into a union of tetrahedral elements using an unstructured meshing method in FEMLAB. Over 500 000 tetrahedral solid elements were created to represent the solid tumor model. The boundary condition was defined at the surface vertices (>800). For each surface vertex on the MRI model, we compute its distances to the surface vertices on the PET model. The closest vertex is the corresponding point. The displacement fields of the surface vertices serve as the boundary motion of the tumor. No additional external force is applied to the tumor model.

The registration approach deforms the tumor surface from the MRI volume toward that from the PET image. The displacements at the surface vertices are the force that drives the elastic surface from MRI toward that from the PET image. The tumor was modeled as a linear isotropic elastic material with Young's modulus of 60 kPa and Poisson's ratio of 0.49.⁴⁵ The FEM model was used to infer volumetric deformation of the tumor from the surface. The force is integrated over each element and is distributed over the nodes belonging to the element using its shape functions. After obtaining the displacement field for all vertices, we used a linear interpolation to obtain the deformed image volume of the tumor.

F. Registration evaluation

A variety of qualitative and quantitative methods were used to evaluate the registration of microPET and high-resolution MRI. First, we used visual inspection methods to evaluate the registration quality. (1) Color overlay displays provide a useful tool to evaluate structure overlap. We have found that rendering one image in gray and the other in red with a manually adjustable transparency scale provides a very good way to visually determine registration accuracy.³⁸ (2) We used a checkerboard display whereby we divided the reference and registered images into sectors and created an output image by alternating sectors from the two input images.³⁷ Even small shifts of edges therefore are clearly visible. (3) We used 3D volume rendering and color overlap to visualize registration results.

Second, quantitative registration errors were computed. (1) We used anatomic landmarks to evaluate the registration results. For example, we found feature landmarks, such as kidneys, on two images and computed the target registration error (TRE), which is the distance after registration between corresponding target points.⁴⁶ (2) We manually segmented the lesion boundaries in image slices and copied them to corresponding slices from other registered volumes.³⁰ From each segmented slice, we compute the center of the lesion. From the segmented boundaries across all slices, we com-

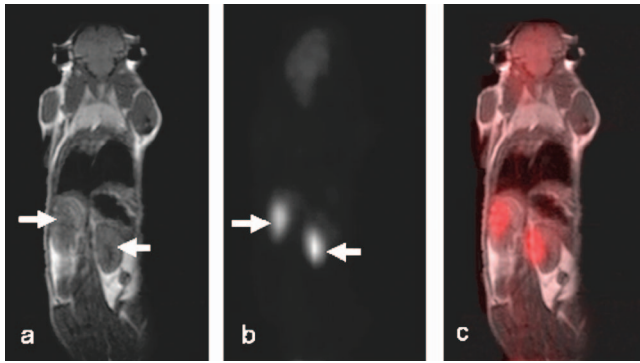


FIG. 2. Visual inspection of whole mouse registration. High-resolution MR image (left) shows the anatomic information of the mouse body. The white arrows indicate the left and right kidneys of the mouse. MicroPET image (center) shows the ^{18}F -FDG distribution within the same mouse. The kidneys (arrows) are well seen on the microPET image. After whole body registration, the overlay of MRI (gray) and microPET (red) shows excellent registration of the mouse body.

pute the centroids of the lesion in 3-D space. This enables offline visual determination of the registration quality. By manually segmenting the lesion from multiple volumes, centroid distances and volume overlap ratios (VORs) are derived to evaluate the registration quality. The VOR is defined as the overlap volume and divided by the average of the volumes measured from MRI and PET images. A VOR value ranges from 0 (no overlap) to 1 (full overlap). (3) We measure the consistency errors for the deformable registration.⁴⁷ We transform a voxel in volume A to volume B and then transform it back to A. The distances between the corresponding voxel after the two deformable transformations serves as a measure of the registration consistent errors.

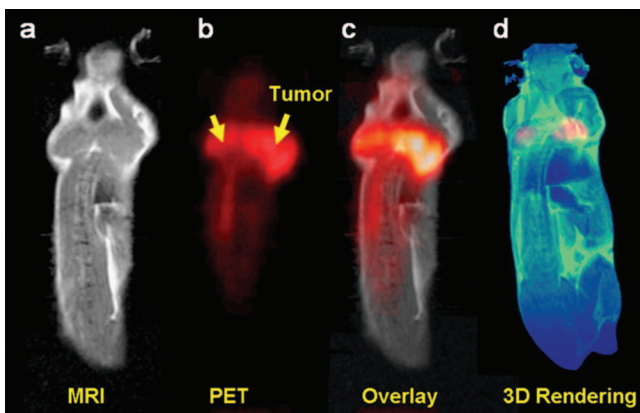


FIG. 3. Three-dimensional registration and fusion of MRI and microPET images. Images from high-resolution MRI (a) and microPET (b) are registered and fused (c). As indicated by the arrow on the microPET image (b), the tumor on the right (control) had greater FDG uptake than the other (treated). On the fused image (c), the MR image (gray) provides the anatomic reference to the microPET image (red). On the 3D rendering image (d), the fusion of the MRI (blue) and microPET (red) shows the 3D distribution of the FDG uptake within the mouse body.

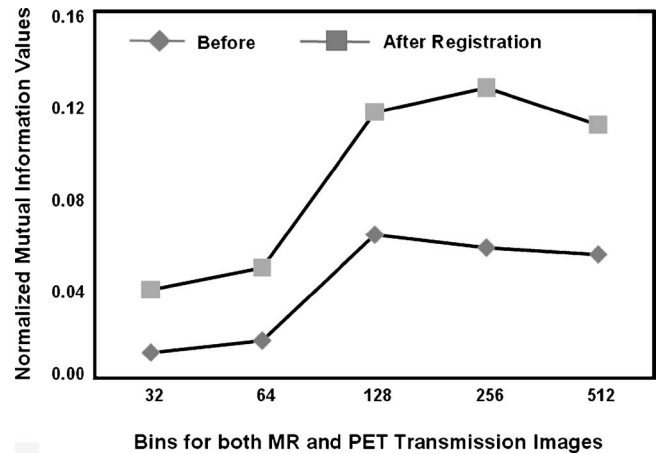


FIG. 4. The effect of intensity scaling on whole body registration. The X axis is the gray levels from 32 to 512. The Y axis is the normalized mutual information (NMI) values between MRI and microPET transmission images. After registration, the NMI values are increased in all cases. At the level of 256, the NMI value is maximal, indicating better registration that is confirmed by visual inspection.

III. RESULTS

A. Results of whole body registration

Figure 2 shows the registration result of a whole mouse body. The MR image provides the anatomic structure of the mouse where the medullary and cortical substances of the kidney are visible. The PET image shows the FDG uptake within the kidneys and renal vessels. The color overlay display shows that the kidneys are aligned. We also examined other slices in different positions and the kidneys were matched in three dimensions. Other organs such as the bladder and heart were also aligned (not shown).

In Fig. 3, we show a fused image and the volume rendering visualization of a mouse body with two tumors. The color overlay provides both anatomic and functional information of the tumors. The MR images provide the anatomic reference to the microPET images. The volume rendering

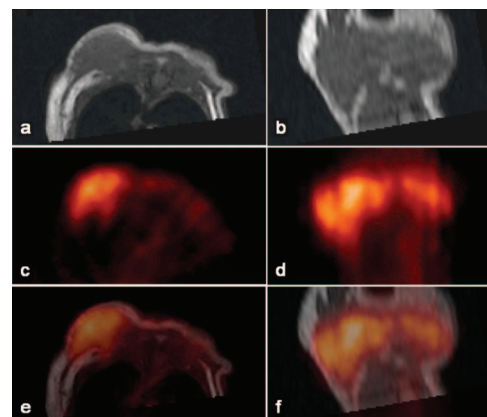


FIG. 5. Fusion of MRI and microPET images in transverse (left) and coronal (right) orientations. Top: MR images that cover the tumor region. Middle: Corresponding PET emission image. Bottom: Color overlay of the MRI (gray) and microPET (red) images. The fusion images show that the tumors were aligned.

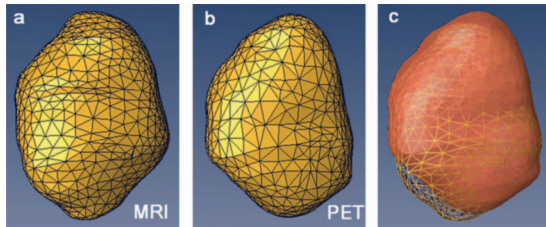


FIG. 6. Three-dimensional meshes of a tumor. (a) Tumor segmented from a high-resolution MR volume. (b) Same tumor from the corresponding microPET emission images. (c) Color overlay of the tumor from MRI (yellow) and microPET (red). The tumor deformed during the two imaging sessions.

displays the distribution of the radioactivity within the whole body. Other visual inspection methods such as boundary overlap showed that the mouse body was registered. We have performed over 40 registration experiments. For three mice, the target registration error is 1.5 ± 0.4 mm, which is comparable to the microPET resolution of about 2 mm.³⁵

We tested the effect of intensity scaling on whole body registration. In Fig. 4, we show the NMI values between the PET transmission and MR image volume. The NMI values increased after registration. When the bin size is 256, the NMI was maximal, indicating the gray level of 256 is best for the whole body registration that was confirmed by the visual inspection.

B. Results of tumor registration

In Fig. 5, we show the results of tumor registration after rigid-body transformation. The color overlay of the MRI and microPET images demonstrates good registration of the tumor in both transverse and coronal slices, indicating that the tumors are aligned in three dimensions.

To evaluate the rigid-body registration of the tumor, we manually segmented it from both MRI and microPET images and then used 3D meshes to represent the tumor surfaces. In Fig. 6, the 3D visualization shows that the tumor deformed between the two imaging sessions. Figure 7 shows two examples where MR image slices and the 3D tumor meshes are simultaneously displayed. In order to evaluate manual segmentation errors, two observers segmented each tumor three times. The volume overlap ratios of the six segmentations are

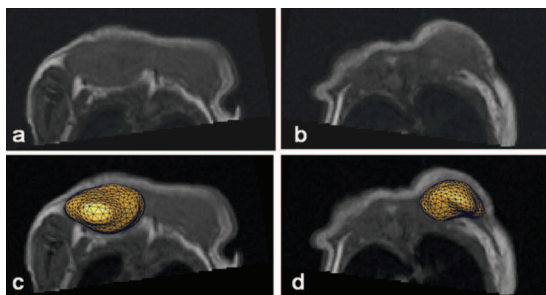


FIG. 7. MR image slices and 3D mesh representation of the tumors. Images on the top are MR image slices that include two tumors. Images at the bottom are the same slices with 3D mesh representation of the tumors. The 3D shapes of the tumors are visible.

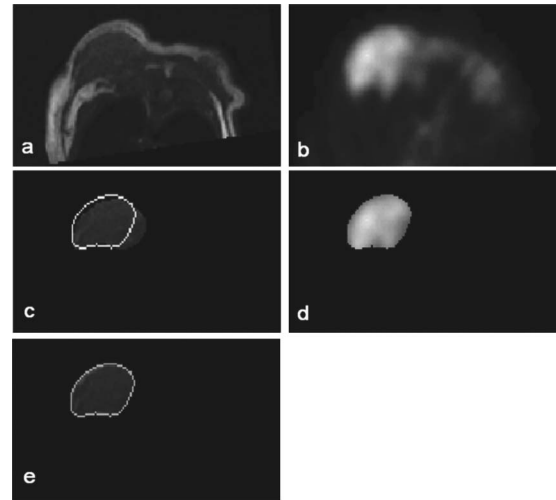


FIG. 8. Comparison of rigid and deformable registration. Images on the top are the corresponding MRI (a) and microPET (b) images after rigid-body registration. The tumor on both images was manually segmented for registration evaluation [(c) and (d)]. The tumor contour from the microPET image (d) is copied to the MR image (c). The contour mismatch is due to the tumor deformation. After deformable registration, the tumor on the MRI is warped and matched with that from the microPET image (e). Other slices are also matched indicating excellent tumor registration in three dimensions.

$95.0\% \pm 1.0\%$ and $92.0\% \pm 2.6\%$ for MRI and PET images, respectively. This indicates excellent repeatability.

In Fig. 8, we compare the results of rigid and deformable registration. The contour overlap shows that the deformable method is better than the rigid-body registration. This is consistent with quantitative measures. The NMI values increased from 0.06 ± 0.01 to 0.12 ± 0.02 after deformable registration. The volume overlap ratios were also improved from $86.3\% \pm 2.5\%$ to $94.7\% \pm 1.5\%$ with deformable registration. The mean consistency error is less than 0.1 mm for the deformable registration.

As shown in Fig. 9, the treated tumor has less FDG uptake than the control, indicating the effect of PDT. This is consistent with the microPET image in Fig. 3. Fusion of PET with MRI aids in defining regions of interest on PET images

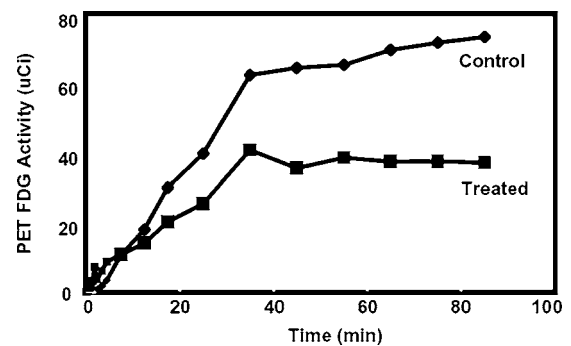


FIG. 9. Uptake of ^{18}F -fluorodeoxyglucose (FDG) for treated and control tumors. The X axis is the time after the injection of FDG. The Y axis is the FDG activity as measured from the microPET images. Immediately after PDT, the treated tumor has a decreased FDG uptake as compared to the control. The difference between the treated and control tumors in the time activity curve indicates the effect of the PDT.

for quantitative measurements. The tumor registration and fusion methods are quite useful for this application. It could provide a powerful tool for other applications of small animal imaging in cancer biology, functional genomics, and drug development.

IV. DISCUSSION

The automatic 3D rigid-body NMI-based method performs well for whole mouse registration. Transmission images are useful for whole body registration. We found that the registration can fail if only PET emission images were used for the calculation of NMI values. The combination of transmission and emission images increased the robustness of whole body registration because the transmission images provide anatomic information of the mouse body and aid in the registration with MR images. However, increasing the percentage of transmission signals from 10% to 100% made no significant difference.

Interestingly, transmission images could not be used for the tumor registration where only a small tumor region was used for the registration. Our experiments showed that even a small percentage (5%) of transmission images would lead to the failure of the tumor registration. We think there may be two reasons: (1) the transmission images are noisy and provide few anatomic details within the tumor region, and (2) the tumor has only a small number of voxels that can be used for the NMI calculation.

The downhill simplex method was selected for the optimization procedure because it performed a little faster than the Powell method in our implementation.³⁶ When the number of image slices is limited, simulated annealing can be another option for MI-based registration.⁴⁸

The deformable registration method is quite accurate for the tumor registration. Because the tumors on both MRI and microPET images were already segmented, the registration quality was well controlled. The deformable registration performs better than the rigid-body method whenever there are deformations of the tumors. Using a Pentium IV computer (3.4 MHz CPU and 3.0 GBytes memory) and FEMLAB program, the computation time for the deformable transformation is less than 4 min.

The MR image quality was excellent because we used a dedicated mouse coil. Though a clinical 1.5 T MR scanner was used for the mouse imaging, we achieved high-resolution MR images for small animal imaging. Future experiments will be performed on two new Bruker Biospec superconducting MR imaging systems (9.4 and 7 T) at our institution.

Tumors respond rapidly to photodynamic therapy, and there is great potential for studying *in vivo* responses with PET and with MRI either during the photoirradiation or within a short time thereafter. It will be important to ensure that changes in metabolic parameters, as measured by PET imaging, are properly assigned to the treated tumor or other tissue of interest. Deformable image registration should improve the ability to quantitatively evaluate the desired responses.

V. CONCLUSIONS

We have developed two registration methods for mouse MRI and microPET images. The NMI-based rigid-body registration was used to align the whole mouse body. The FEM-based deformable registration method was developed to register the tumors. The image registration and fusion provided both functional and anatomic information for evaluating photodynamic therapy in mice. These methods could provide a useful tool for other applications in small animal, cellular, and molecular imaging.

ACKNOWLEDGMENTS

The algorithm developed in this research was partially supported by the DoD Award DAMD17-02-1-0230, the Northeastern Ohio Animal Imaging Resource Center as funded by NIH Grant No. 5R24CA110943, and the Case Comprehensive Cancer Center Pilot Project Award.

^{a)}Electronic mail: baowei.fe@case.edu

¹T. J. Dougherty, "An update on photodynamic therapy applications," *J. Clin. Laser Med. Surg.* **20**, 3–7 (2002).

²B. W. Fei, R. Muzic, Z. Lee, C. Flask, R. Morris, J. L. Duerk, and D. L. Wilson, "Registration of micro-PET and high resolution MR images of mice for monitoring photodynamic therapy," *Proceeding of SPIE on Medical Imaging: Physiology, Function, and Structure from Medical Images* (2004), pp. 371–379.

³D. Lapointe, N. Brasseur, J. Cadorette, C. La Madeleine, S. Rodrigue, J. E. van Lier, and R. Lecomte, "High-resolution PET imaging for *in vivo* monitoring of tumor response after photodynamic therapy in mice," *J. Nucl. Med.* **40**, 876–882 (1999).

⁴B. G. Winsborrow, H. Grondey, H. Savoie, C. A. Fyfe, and D. Dolphin, "Magnetic resonance imaging evaluation of photodynamic therapy-induced hemorrhagic necrosis in the murine M1 tumor model," *Photochem. Photobiol.* **66**, 847–852 (1997).

⁵S. Gross, A. Gilead, A. Scherz, M. Neeman, and Y. Salomon, "Monitoring photodynamic therapy of solid tumors online by BOLD-contrast MRI," *Nat. Med.* **9**, 1327–1331 (2003).

⁶S. D. Kennedy, L. S. Szczepaniak, S. L. Gibson, R. Hilf, T. H. Foster, and R. G. Bryant, "Quantitative MRI of Gd-DTPA uptake in tumors: response to photodynamic therapy," *Magn. Reson. Med.* **31**, 292–301 (1994).

⁷J. Mattiello, J. L. Evelhoch, E. Brown, A. P. Schaap, and F. W. Hetzel, "Effect of photodynamic therapy on RIF-1 tumor metabolism and blood flow examined by 31P and 2H NMR spectroscopy," *NMR Biomed.* **3**, 64–70 (1990).

⁸J. C. Bremner, S. R. Wood, J. K. Bradley, J. Griffiths, G. E. Adams, and S. B. Brown, "31P magnetic resonance spectroscopy as a predictor of efficacy in photodynamic therapy using differently charged zinc phthalocyanines," *Br. J. Cancer* **81**, 616–621 (1999).

⁹Q. Jiang, M. Chopp, and F. W. Hetzel, "In vivo 31P NMR study of combined hyperthermia and photodynamic therapies of mammary carcinoma in the mouse," *Photochem. Photobiol.* **54**, 795–799 (1991).

¹⁰Y. H. Liu, R. M. Hawk, and S. Ramaprasad, "In vivo relaxation time measurements on a murine tumor model—prolongation of T1 after photodynamic therapy," *Magn. Reson. Imaging* **13**, 251–258 (1995).

¹¹V. Plaks, N. Koudinova, U. Nevo, J. H. Pinthus, H. Kanety, Z. Eshhar, J. Ramon, A. Scherz, M. Neeman, and Y. Salomon, "Photodynamic therapy of established prostatic adenocarcinoma with TOOKAD: a biphasic apparent diffusion coefficient change as potential early MRI response marker," *Neoplasia* **6**, 224–233 (2004).

¹²T. C. Zhu, E. Glatstein, S. M. Hahn, A. Dimofte, J. C. Finlay, D. Stripp, T. Busch, J. Miles, R. Whittington, S. B. Malkowicz, and Z. Tochner, "Optical properties of human prostate at 732 nm measured *in vivo* during motexafin lutetium-mediated photodynamic therapy," *Photochem. Photobiol.* **81**, 96–105 (2004).

¹³R. A. Weersink, J. Forbes, S. Bisland, J. Trachtenberg, M. Elhilali, P. H. Brun, and B. C. Wilson, "Assessment of cutaneous photosensitivity of

- TOOKAD (WST09) in pre-clinical animal models and in patients," *Photochem. Photobiol.* **81**, 106–113 (2004).
- ¹⁴J. Cizek, K. Herholz, S. Vollmar, R. Scharder, J. Klein, and W. D. Heiss, "Fast and robust registration of PET and MR images of human brain," *Neuroimage* **22**, 434–442 (2004).
- ¹⁵R. Myers, "The application of PET-MR image registration in the brain," *Br. J. Radiol.* **75**, S31–S35 (2002).
- ¹⁶W. M. Wells III, P. Viola, H. Atsumi, S. Nakajima, and R. Kikinis, "Multi-modal volume registration by maximization of mutual information," *Med. Image Anal.* **1**, 35–51 (1996).
- ¹⁷J. C. Wong, C. Studholme, D. J. Hawkes, and M. N. Maisey, "Evaluation of the limits of visual detection of image misregistration in a brain fluorine-18 fluorodeoxyglucose PET-MRI study," *Eur. J. Nucl. Med.* **24**, 642–650 (1997).
- ¹⁸C. Studholme, D. L. Hill, and D. J. Hawkes, "Automated three-dimensional registration of magnetic resonance and positron emission tomography brain images by multiresolution optimization of voxel similarity measures," *Med. Phys.* **24**, 25–35 (1997).
- ¹⁹L. Thurfjell, Y. H. Lau, J. L. Andersson, and B. F. Hutton, "Improved efficiency for MRI-SPET registration based on mutual information," *Eur. J. Nucl. Med.* **27**, 847–856 (2000).
- ²⁰S. J. Kiebel, J. Ashburner, J. B. Poline, and K. J. Friston, "MRI and PET coregistration—a cross validation of statistical parametric mapping and automated image registration," *Neuroimage* **5**, 271–279 (1997).
- ²¹N. Hayakawa, K. Uemura, K. Ishiwata, Y. Shimada, N. Ogi, T. Nagaoka, H. Toyama, K. Oda, A. Tanaka, K. Endo, and M. Senda, "A PET-MRI registration technique for PET studies of the rat brain," *Nucl. Med. Biol.* **27**, 121–125 (2000).
- ²²D. J. Rubins, W. P. Melega, G. Lacan, B. Way, A. Plenevaux, A. Luxen, and S. R. Cherry, "Development and evaluation of an automated atlas-based image analysis method for microPET studies of the rat brain," *Neuroimage* **20**, 2100–2118 (2003).
- ²³Y. Shimada, K. Uemura, B. A. Ardekani, T. Nagaoka, K. Ishiwata, H. Toyama, K. Ono, and M. Senda, "Application of PET-MRI registration techniques to cat brain imaging," *J. Neurosci. Methods* **101**, 1–7 (2000).
- ²⁴W. R. Crum, T. Hartkens, and D. L. Hill, "Non-rigid image registration: theory and practice," *Br. J. Radiol.* **77**(Spec. No. 2), S140–S153 (2004).
- ²⁵M. Ferrant, A. Nabavi, B. Macq, F. A. Jolesz, R. Kikinis, and S. K. Warfield, "Registration of 3-D intraoperative MR images of the brain using a finite-element biomechanical model," *IEEE Trans. Med. Imaging* **20**, 1384–1397 (2001).
- ²⁶M. I. Miga, K. D. Paulsen, P. J. Hoopes, F. E. Kennedy, Jr., A. Hartov, and D. W. Roberts, "In vivo quantification of a homogeneous brain deformation model for updating preoperative images during surgery," *IEEE Trans. Biomed. Eng.* **47**, 266–273 (2000).
- ²⁷T. Zhang, N. P. Orton, T. R. Mackie, and B. R. Paliwal, "Technical note: A novel boundary condition using contact elements for finite element based deformable image registration," *Med. Phys.* **31**, 2412–2415 (2004).
- ²⁸A. Bharatha, M. Hirose, N. Hata, S. K. Warfield, M. Ferrant, and K. H. Zou, "Three-dimensional finite element-based deformable registration of pre- and intraoperative prostate imaging," *Radiology* **221**, 224 (2001).
- ²⁹A. I. Veress, J. A. Weiss, G. T. Gullberg, D. G. Vince, and R. D. Rabbitt, "Strain measurement in coronary arteries using intravascular ultrasound and deformable images," *J. Biomech. Eng.* **124**, 734–741 (2002).
- ³⁰B. W. Fei, C. Kemper, and D. L. Wilson, "A comparative study of warping and rigid body registration for the prostate and pelvic MR volumes," *Comput. Med. Imaging Graph.* **27**, 267–281 (2003).
- ³¹J. Lian, L. Xing, S. Hunjan, C. Dumoulin, J. Levin, A. Lo, R. Watkins, K. Rohling, R. Giaquinto, D. Kim, D. Spielman, and B. Daniel, "Mapping of the prostate in endorectal coil-based MRI/MRSI and CT: a deformable registration and validation study," *Med. Phys.* **31**, 3087–3094 (2004).
- ³²H. Wang, L. Dong, M. F. Lii, A. L. Lee, R. de Crevoisier, R. Mohan, J. D. Cox, D. A. Kuban, and R. Cheung, "Implementation and validation of a three-dimensional deformable registration algorithm for targeted prostate cancer radiotherapy," *Int. J. Radiat. Oncol., Biol., Phys.* **61**, 725–735 (2005).
- ³³C. R. Meyer, J. L. Boes, B. Kim, P. H. Bland, K. R. Zasadny, P. V. Kison, K. Koral, K. A. Frey, and R. L. Wahl, "Demonstration of accuracy and clinical versatility of mutual information for automatic multimodality image fusion using affine and thin-plate spline warped geometric deformations," *Med. Image Anal.* **1**, 195–206 (1997).
- ³⁴S. I. Zaidi, N. L. Oleinick, M. T. Zaim, and H. Mukhtar, "Apoptosis during photodynamic therapy-induced ablation of RIF-1 tumors in C3H mice: electron microscopic, histopathologic and biochemical evidence," *Photochem. Photobiol.* **58**, 771–776 (1993).
- ³⁵C. Knoess, S. Siegel, A. Smith, D. Newport, N. Richerzhagen, A. Winkler, A. Jacobs, R. N. Goble, R. Graf, K. Wienhard, and W. D. Heiss, "Performance evaluation of the microPET R4 PET scanner for rodents," *Eur. J. Nucl. Med.* **30**, 737–747 (2003).
- ³⁶B. W. Fei, A. Wheaton, Z. Lee, J. L. Duerk, and D. L. Wilson, "Automatic MR volume registration and its evaluation for the pelvis and prostate," *Phys. Med. Biol.* **47**, 823–838 (2002).
- ³⁷B. W. Fei, J. L. Duerk, and D. L. Wilson, "Automatic 3D registration for interventional MRI-guided treatment of prostate cancer," *Comput. Aided Surg.* **7**, 257–267 (2002).
- ³⁸B. W. Fei, Z. Lee, J. L. Duerk, J. S. Lewin, D. B. Sodee, and D. L. Wilson, "Registration and fusion of SPECT, high resolution MRI, and interventional MRI for thermal ablation of the prostate cancer," *IEEE Trans. Nucl. Sci.* **51**, 177–183 (2004).
- ³⁹B. Fei, J. L. Duerk, D. T. Boll, J. S. Lewin, and D. L. Wilson, "Slice-to-volume registration and its potential application to interventional MRI-guided radio-frequency thermal ablation of prostate cancer," *IEEE Trans. Med. Imaging* **22**, 515–525 (2003).
- ⁴⁰B. W. Fei, Z. H. Lee, D. T. Boll, J. L. Duerk, J. S. Lewin, and D. L. Wilson, "Image registration and fusion for interventional MRI guided thermal ablation of the prostate cancer," *Medical Image Computing and Computer-Assisted Intervention-Miccai 2003, Pt 2* (2003), Vol. 2879, pp. 364–372.
- ⁴¹J. P. Plum, J. B. Maintz, and M. A. Viergever, "Mutual-information-based registration of medical images: a survey," *IEEE Trans. Med. Imaging* **22**, 986–1004 (2003).
- ⁴²F. Maes, A. Collignon, D. Vandermeulen, G. Marchal, and P. Suetens, "Multimodality image registration by maximization of mutual information," *IEEE Trans. Med. Imaging* **16**, 187–198 (1997).
- ⁴³B. W. Fei, Z. Lee, J. L. Duerk, and D. L. Wilson, "Image registration for interventional MRI guided procedures: Similarity measurements, interpolation methods, and applications to the prostate," *Lect. Notes Comput. Sci.* **2717**, 321–329 (2003).
- ⁴⁴J. Nelder and R. A. Mead, "A simplex method for function minimization," *Comput. J.* **7**, 308–313 (1965).
- ⁴⁵T. A. Krouskop, T. M. Wheeler, F. Kallel, B. S. Garra, and T. Hall, "Elastic moduli of breast and prostate tissues under compression," *Ultrasound Imaging* **20**, 260–274 (1998).
- ⁴⁶J. M. Fitzpatrick and J. B. West, "The distribution of target registration error in rigid-body point-based registration," *IEEE Trans. Med. Imaging* **20**, 917–927 (2001).
- ⁴⁷J. He and G. E. Christensen, "Large deformation inverse consistent elastic image registration," *Inf. Process. Med. Imaging* **18**, 438–449 (2003).
- ⁴⁸X. Li, P. Zhang, R. Brisman, and G. Kutcher, "Use of simulated annealing for optimization of alignment parameters in limited MRI acquisition volumes of the brain," *Med. Phys.* **32**, 2363–2370 (2005).

Fei BW, Wang H, Muzic RF Jr, Flask CA, Wilson DL, Duerk JL, Feyes DK, Oleinick NL. Deformable and rigid registration of MRI and microPET images for photodynamic therapy of cancer in mice. *Medical Physics* 2006;33:753-760.

Copyright 2006 Am. Assoc. Phys. Med. One print or electronic copy may be made for personal use only. Systematic reproduction and distribution, duplication of any material in this paper for a fee or for commercial purposes, or modification of the content of the paper are prohibited.